Noise Control Capability of Structurally Integrated Resonator Arrays in a Foam-Treated Cylinder

Albert Allen and Noah Schiller
NASA Langley Research Center

Jerry Rouse
Sandia National Laboratories

ABSTRACT

Corrugated-core sandwich structures with integrated acoustic resonator arrays have been of recent interest for launch vehicle noise control applications. Previous tests and analyses have demonstrated the ability of this concept to increase sound absorption and reduce sound transmission at low frequencies. However, commercial aircraft manufacturers often require fibrous or foam blanket treatments for broadband noise control and thermal insulation. Consequently, it is of interest to further explore the noise control benefit and trade-offs of structurally integrated resonators when combined with various degrees of blanket noise treatment in an aircraft-representative cylindrical fuselage system.

In this study, numerical models were developed to predict the effect of broadband and multi-tone structurally integrated resonator arrays on the interior noise level of cylindrical vibroacoustic systems. Foam layers with a range of thicknesses were applied near the inside surface of the cylinder to represent different degrees of conventional blanket treatments. Excitations including point force as well as harmonic and random fluctuating pressure fields were considered. The results suggest that structurally integrated resonators can be tuned to address a variety of noise control requirements and effectively used in conjunction with foam blanket noise treatments, but their relative benefit is reduced when thicker foam treatments are used.

INTRODUCTION

High interior noise levels in aerospace vehicles can damage sensitive equipment, lead to crew hearing loss, and annoy passengers. While high-frequency noise can often be attenuated with conventional fibrous and foam blanket treatments, low-frequency noise is much more difficult to control without thick, heavy treatment. Passive acoustic resonators, however, have the potential to provide effective low frequency noise control. Helmholtz resonator, quarter-wave resonators, and variations thereof have seen widespread use in the field of building acoustics. In practice, they are typically combined into arrays of similarly tuned resonators to reduce noise at particular frequencies, or varied in tuning to target a wider band of frequencies. If installed into or alongside a wall, the resonators achieve noise reduction by increasing the absorption of the adjacent acoustic volume, but can also improve the transmission loss of the wall [1].

A succesful example of passive resonant noise control within the aerospace industry is the use of perforate-over-honeycomb acoustic liners along the interior walls of aircraft engine nacelles to reduce fan noise. In simplistic terms, the performance of this type of liner is controlled by honeycomb cell depth and perforated face sheet resistance. Manufacturing constraints have previously limited the variety of achievable cell depths in production liners, but recent developments have demonstrated the ability, through advanced manufacturing techniques, to create variable depth liners that can meet a wide range of noise control requirements [2]. These developments have influenced the work described here.

There are relatively few examples of the use of passive acoustic resonators for aircraft *interior* noise control. A series of efforts were carried out during the late 1980's and early '90's dealing with passive resonator arrays placed within a double wall (fuselage and trim) configuration. Mason and Fahy applied Helmholtz resonators along the perimeter of a flat double wall assembly to reduce transmission within a narrow frequency range near the double wall mass-air-mass resonance [3]. Their results showed that significant improvements to transmission loss can be made when the resonators were tuned to target a narrow range of frequencies. Shortly thereafter, Prydz et al. developed transfer matrix-based analytical methods to account for arrays of Helmholtz resonators installed in a trim panel assembly [4]. Kuntz et al. later demonstrated a 5-6 dB flight test noise reduction in the interior of a propfan driven aircraft (Gulfstream II) by installing an array of Helmholtz resonators between fuselage and trim panels [5]. However, the authors also mentioned the limitations of trim-

based treatments due to short-circuit paths from the fuselage structure to the interior via “storage compartments, air-conditioning ducts, racks, and galleys”.

The practical use of supplemental or “add-on” resonators able to provide substantial interior noise control at lower frequencies where foam and fiber treatments perform poorly is limited due to size and weight constraints. However, the integration of long “quarter-wave” resonators into existing primary fuselage structures could alleviate these limitations. Along these lines, researchers from the Air Force Research Laboratory and the University of Pittsburg have recently studied chamber core sandwich structures with integrated acoustic resonators [6, 7]. They demonstrated that the noise reduction of a chamber core cylinder with integrated resonators could be increased at targeted frequencies. Tuned Chamber Core (TCC) is a similar concept recently studied for application in launch vehicle payload fairings [8]. An exploded view drawing and corresponding photo of a composite test article containing 138 resonators from [8] are shown in Figure 1. Improvements in both transmission loss and absorption were achieved around the targeted frequencies (200 Hz to 315 Hz) during standard ASTM E90 and C423 laboratory measurements. However, it is important to also mention that an increase in transmission was evident at higher frequencies due to the additional transmission path through the acoustically large inlets. This may not be a concern for many applications involving conventional blanket treatments, though, as the performance of conventional blankets often exceeds the noise requirements at higher frequencies.

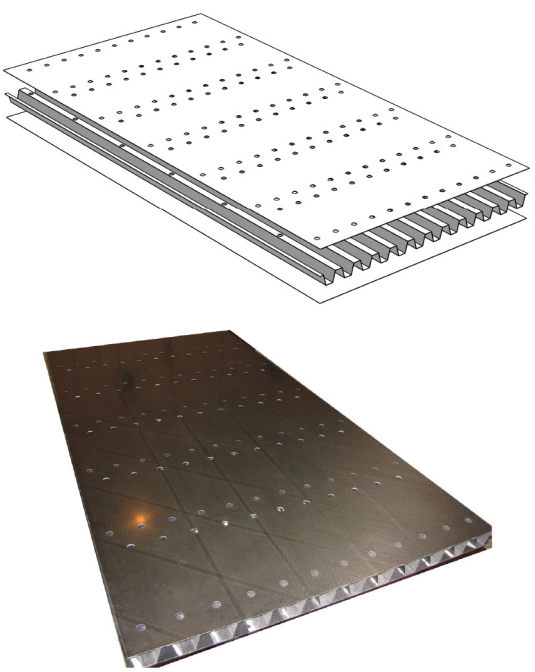

Figure 1. Exploded view drawing and photo of the 1.219 m by 2.438 m TCC test panel from [8].

Generally speaking, TCC and related concepts require that the primary fuselage or fairing structure be of a corrugated-core sandwich design (or similar fluted-core, Z-core, box-core, etc. design). Inlets are machined at particular locations on the interior face sheet and end-caps are inserted (or co-bonded) into the core chambers at specific locations to create an array of tuned acoustic resonators. For a given application, it is envisioned that the chamber and inlet geometries would be designed to provide a desired noise reduction spectrum while also maintaining load bearing capabilities. While the ability of these structures to contain arrays of tunable, low frequency performing resonators without an appreciable increase in weight or reduced interior volume is of particular interest here, one can also imagine additional nonacoustic possibilities, such as fuselage integrated system wiring, environmental control system ducting, or thermal treatments.

This paper examines the benefits and relative trade-offs of conventional foam blanket and structurally integrated resonator array noise treatments in a corrugated-core cylinder using numerical modeling methods. The cylinder considered is representative in diameter of a regional airliner fuselage section. A description of the approach used when creating the numerical models is given. Details pertaining to how the corrugated-core structure and resonator arrays were represented in the model are also described. The noise control capability of the resonator array is a function of the input impedance of each resonator in the array. Consequently, a model of the resonator impedance is also described along with experimental evaluations. Finally, the model is exercised while considering different foam blanket treatments, resonator array configurations, and excitations and the resulting noise reductions (NR) attributed to each treatment are discussed.

MODELING

The following sections describe the finite element model of the cylindrical vibroacoustic system, and include details pertaining to how the corrugated-core structure and resonator arrays were represented in the model.

Cylindrical Vibroacoustic System

Finite element (FE) models consisting of a cylinder structure with interior and exterior acoustic systems and various thicknesses of foam blanket treatments were developed for analyses using a commercial FE software [9]. The cylinder is 2.6 m long with a diameter of 2.734 m. This diameter is representative of a regional airliner fuselage. An example of the FE model is shown in Figure 2*. While an FE modeling approach is more computationally expensive relative to other prediction methods, it was found to be tractable within the frequency range of interest (below ~500 Hz) through the use of parallelization.

The interior acoustic system was comprised of AC3D20 quadratic hexahedral elements with standard condition properties (ρ = 1.21 kg/m^3, c = 343 m/s). An additional foam blanket region near the inner surface of the cylinder was also modeled using AC3D20 elements, but frequency dependent complex effective densities and bulk moduli were used in this case. The foam properties were determined using Miki’s equivalent fluid model and a lightweight 6 kg/m^3 blend of melamine with a flow resistivity of 9400 Pa·s/m^2 was assumed [10, 11]. Hard wall boundaries were applied to the acoustic volume at the top and bottom of the cylinder. The cylinder was modeled with thick shell S8R quadratic quadrilateral elements and had an untreated mass of

approximately 162 kg. No structural boundary conditions were applied to the cylinder, i.e., it was modeled as "free hanging". To account for the mass of the foam, additional nonstructural masses were applied to all foam-coupled shell elements. Energy lost due to exterior sound radiation was accounted for with an infinite radiation boundary condition, which was realized by wrapping the cylinder with two layers of acoustic elements and an outer layer of ACIN3D8 quadratic infinite acoustic elements. This abbreviated exterior boundary condition was used to approximate the radiation impedance imposed upon the outer surface of the cylinder. Because detailed knowledge of the exterior sound field was not needed, a more precise representation involving a spherical exterior volume was deemed unnecessary.

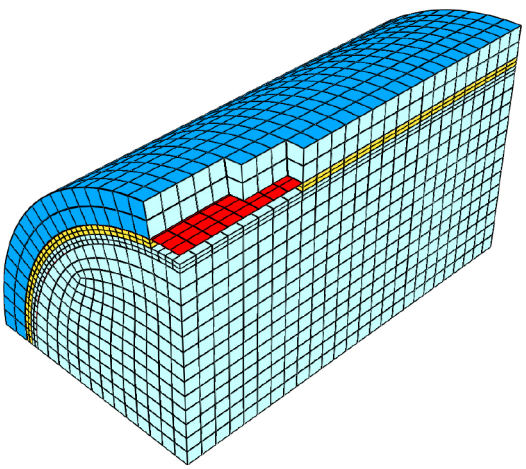

Figure 2. Cutaway view of cylinder FE model with 51 mm thick foam treatment. Acoustic elements shown in light blue, equivalent fluid foam elements in yellow, infinite acoustic elements in dark blue, and cylinder shell elements in red.

Structural-acoustic and acoustic-acoustic "tie" constraints were specified at the surfaces between shell and acoustic regions and between the interior acoustic volume and an annular region near the foam treatment. The acoustic-acoustic tie was utilized simply for rapid mesh refinement near the cylinder wall. This improved the convergence rate of the model by better resolving the relatively high wavenumbers within the foam and direct acoustic field of the cylinder. The structural-acoustic tie, on the other hand, coupled the normal velocities of the vibrating structure to pressure at the interfaces between acoustic medium and structure.

The analysis was partitioned into multiple bands from the 40 Hz to 500 Hz 1/3 octaves. The element sizing was specified to provide at least 8 quadratic elements per wavelength in the acoustic regions at the highest frequency in each band of analysis.

Corrugated-Core Sandwich Structure

A notional corrugated-core configuration was assumed for the purposes of this study. The structure is comprised of aluminum (E = 70 GPa, ρ = 2700 kg/m^3, ν = 0.33) with uniform 1 mm thick elements as depicted in the cross-section schematic of Figure 3. The area density of this structure is 7.2 kg/m^2.

To reduce model size, homogenized shell properties were used in lieu of modeling the detailed corrugated-core geometry. In-plane elastic constants $E1$, $E2$, $\nu 12$, and $G12$ were defined for the homogenized shell while assuming orthotropic elastic behavior under plane stress. Transverse shear moduli $G13$ and $G23$ were also included. While a starting point for the estimation of these properties was informed from previous derivations by Lok [12], they were ultimately determined through trial and error by comparing eigensolution results of homogenized shell cylinders with explicitly modeled corrugated-core cylinders as shown in Figure 4.† The homogenized shell properties listed in Table 1 were found to adequately represent the stiffness characteristics of the corrugated-core structure selected for this study.

Table 1. Corrugated-core homogenized shell properties.

thickness	30 mm	$\nu 12$	0.33
ρ	240 kg/m^3	$G12$	5.8 GPa
$E1$	4.9 GPa	$G13$	0.9 GPa
$E2$	7.8 GPa	$G23$	1.9 MPa

Resonator Impedance

As previously described, the core of the sandwich structure is partitioned into long cavities that can be used as acoustic resonators. A schematic of a single resonator is depicted in Figure 5. An inlet is created for each resonator by drilling a hole in the inside facesheet near one end of the cavity. Since the inlets are compact relative to the acoustic wavelength (within the frequency range of interest), the resonators are considered locally reacting and their effect on the interior acoustic field can be modeled as a surface impedance or admittance boundary condition in the vicinity of the resonator inlet. This assumption eliminates the need to explicitly model the core and cavity within a finite element modeling context.

The impedance model used in this work includes a term that accounts for the cavity and a separate term that accounts for the inlet. The specific acoustic impedance of the cavity below the frequency at which cross-section duct modes occur can be found using a one-dimensional plane-wave analysis as

$$z_c = \frac{-j\rho c S_i}{S_c} \cot\left(k_c L_c\right), \tag{1}$$

where ρ and c are the ambient density and speed of sound, respectively, S_i is the area of the inlet, S_c is the cross-section area of the cavity, L_c is the length of the cavity, and $k_c = \omega/c + (1 - j)\,\alpha_c$ is the complex wavenumber. The attenuation constant, α_c, accounts for thermal and viscous losses along the cavity walls and is defined using a wide-duct boundary layer absorption model as

$$\alpha_c = \frac{1}{r_c}\sqrt{\frac{\omega\mu}{2\rho c^2}}\left(1 + \frac{\gamma - 1}{\sqrt{\mathrm{Pr}}}\right). \tag{2}$$

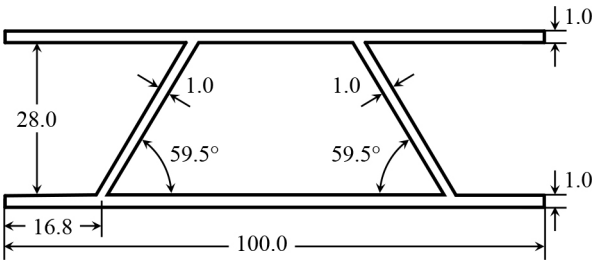

Figure 3. Cross section of the notional corrugated-core sandwich structure (unit = mm).

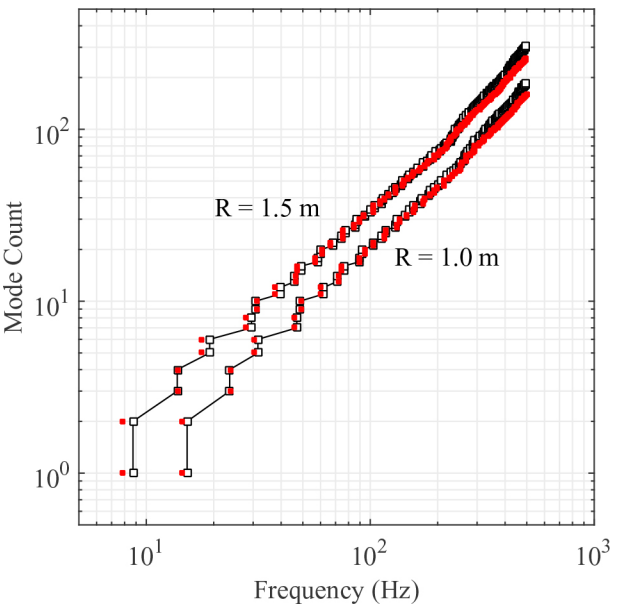

Figure 4. Mode count of the detailed corrugated-core cylinder (□) compared with the homogenized shell cylinder (■). Cylinders with radii of 1.0 m and 1.5 m and heights of 1.5 m were considered.

In the equation above, $r_c = \sqrt{S_c/\pi}$ is the effective radius of the cavity, μ is the dynamic viscosity of the fluid, γ is the ratio of heat capacities, and Pr is the Prandtl number [13]. The specific acoustic impedance of the inlet is modeled as

$$z_i = j\omega\rho L_n, \tag{3}$$

where L_n is the effective neck length. For thin walls, the effective length is approximately equal to the face sheet thickness plus an additional $8r/(3\pi)$ to account for the inward-directed end correction of the inlet [13]. Using the acoustic circuit analogy, the total input impedance of the resonator is the component impedances combined in series given by

$$z_r = z_i + z_c + R, \tag{4}$$

where R is a resistance term that accounts for other losses not captured by the wide-duct boundary layer absorption model, such as near-inlet vortex shedding or losses introduced by an additional resistive mesh placed over the inlet. An experimental evaluation of the aforementioned resonator input impedance model is provided in the appendix.

The resonator arrays were modeled as admittance boundary conditions applied along the interior surface of the cylinder,

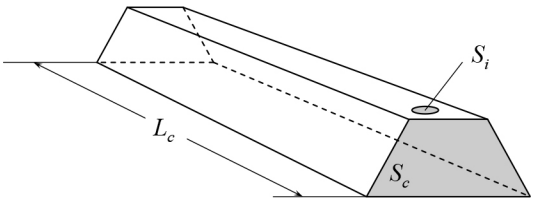

Figure 5. Schematic of a single resonator in a trapezoidal core.

where admittance is defined as $y_r = 1/z_r$. This type of boundary condition can be described using the mechanical analogy as series-connected complex springs distributed in parallel between the structure and acoustic medium. Defining the admittance separately at each resonator inlet would lead to an overly complex and large FE model. Consequently, the resonators were represented in the model by using area averaged admittance boundary conditions. It is then useful to consider a resonator array unit cell which contains a variety of resonators with chamber lengths corresponding to the desired noise reduction requirement. The area averaged specific acoustic admittance $\langle y \rangle$ of a unit cell resonator array including n resonators was determined using

$$\langle y \rangle = \frac{y_w S_w + \sum_{p=1}^{n} y_{rp} S_{ip}}{S_w + \sum_{p=1}^{n} S_{ip}} \tag{5}$$

where y_w and S_w refer respectively to the admittance and surface area of the interior facing cylinder wall (not including resonator inlets) and y_{rp} and S_{ip} refer respectively to the admittance and inlet area of each resonator. The untreated interior wall of the cylinder was assumed to contribute a small amount of absorption, so y_w was assigned values corresponding to a normal incidence absorption coefficient of 0.05.

Analysis

The previously described model was exercised while considering three different excitations: 1) a harmonic point load, 2) a random diffuse field, and 3) a harmonic multitone field originating from two nearby monopoles with locations representative of turboprops. The first two cases consisted of broadband excitations with no spectral shaping, so a resonator array with a wide variety of chamber lengths was conceptualized to provide broadband performance between 100 Hz and 500 Hz. The multitone excitation included a shaped signature characteristic of noise produced by the turboprops of a regional aircraft. In this case, the resonator array was tuned to target specific frequencies near the multitones (85 Hz, 170 Hz, 255 Hz, and 340 Hz) rather than spread evenly over a wide frequency range.

The broadband and multitone resonator array unit cells are shown in Figure 6 and their corresponding area averaged impedances, $\langle z \rangle = 1/\langle y \rangle$, are shown in Figure 7. In both cases, a baseline resistance R of 2 MKS Rayl was added when calculating $\langle y \rangle$, which corresponds to the experimental results described in the appendix.

However, the admittance spectrum of the broadband array was further smoothed by adding an additional 10 MKS Rayl to R (12 MKS Rayl in total) in order to flatten the impedance spectrum and uniformly distribute the influence from approximately 100 Hz to 500 Hz. This added resistance can be physically realized by adding a wire mesh or perforated facing sheet over the resonator inlets.

To study the performance of the resonator array in conjunction with various thicknesses of conventional blanket treatments, foam layers with thicknesses of 25.4 mm, 50.8 mm, 101.6 mm, and 152 mm were applied uniformly along the interior surface of the cylinder. Variation of the structural damping was not considered and a frequency independent material loss factor of 2% was applied to the shell property. It is worth noting, however, that the foam treatments were found to impart a significant amount of effective damping to the cylinder response upon viewing the results. Trim paneling was not included in the model.

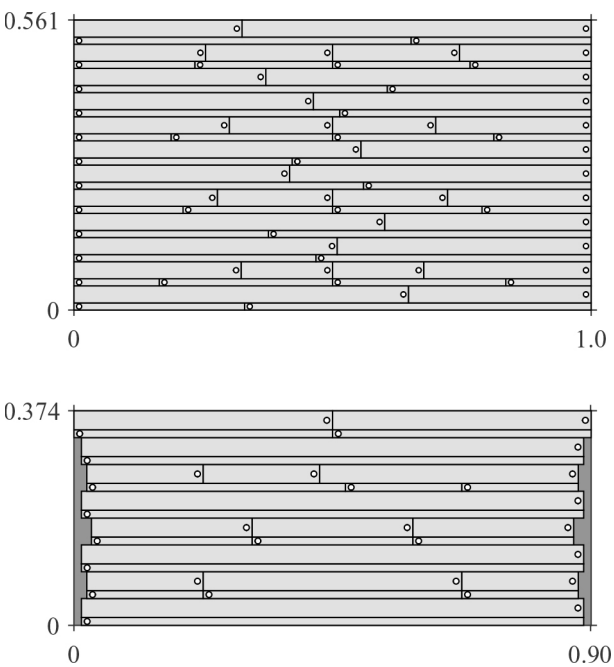

Figure 6. Broadband (top) and multitone (bottom) tuned resonator array unit cells.

Direct frequency domain analyses were performed as opposed to modal domain methods. This was chosen to ensure strong coupling between the cylinder and adjacent acoustic mediums and to accurately model the wave propagation through the lossy, bulk reacting foam regions adjacent to the cylinder wall. For the harmonic point force case, the excitation was simply applied along the cylinder exterior as a concentrated point force. For the load case involving two multitone monopole sources located on either side of the cylinder, frequency dependent complex surface pressures were specified at each element along the outer surface of the cylinder. Scattering due to the rigid body cylinder was accounted for using the boundary element method prior to FE analyses in this case. For the random diffuse field case, an ensemble of 5 pressure field instances was applied for each configuration as complex surface pressures in a sampling procedure [14]. Each diffuse field instance was created by using the plane wave summation method, where spherically uniform distributed incident waves with random phases are summed [15]. To facilitate comparative analyses, a fixed random seed was applied so that field instances were varied randomnly relative to each other for a given configuration, but the same ensemble of field instances were applied across configurations. Scattering due to the cylinder was neglected for the diffuse field load cases.

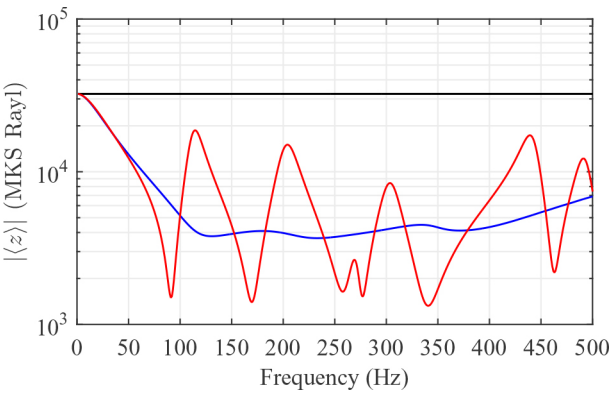

Figure 7. The absolute value of the area averaged impedance $|\langle z \rangle|$ of the broadband (—) and multi-tone (—) resonator array unit cells. The baseline wall impedance corresponding to a normal incidence absorption coefficient of 0.05 is also shown for comparison (—).

Ultimately, the interior space averaged sound pressure level $\langle L_p \rangle$ was calculated by averaging the mean square pressure at nodes within an inner cylindrical region extending to 28 cm from the cylinder wall. To avoid biases in $\langle L_p \rangle$ due to changes in the FE mesh from model to model, the pressures were averaged in a volume weighted sense by

$$\langle L_p \rangle = 10 \log_{10} \left(\frac{\sum_n \left(\left(\frac{|p_n|}{\sqrt{2}} \right)^2 V_n \right)}{\sum_n V_n} \Big/ p_{ref}^2 \right), \tag{6}$$

where p_n are the resulting interior nodal pressures, V_n are the corresponding nodal volumes, and $p_{ref} = 20\ \mu$Pa is the reference pressure.

RESULTS

For the first load case, an inward directed harmonic point force was applied along the side of the cylinder located 1/3 of the cylinder height away from one edge. This excitation is representative of a structure-borne noise source. The change in interior noise level $\langle L_p \rangle$ attributed to the resonator array (while holding the foam treatment constant) was determined as

$$\mathrm{NR} = \langle L_p \rangle_A - \langle L_p \rangle_B, \tag{7}$$

where A and B denote application of y_w and $\langle y \rangle$ admittance boundary conditions along the cylinder interior surface, respectively. In other words, NR is the interior noise reduction due to opening the otherwise closed resonator inlets. The results are shown on a 1/3 octave basis in Figure 8 for various foam thicknesses.‡

Resonator lengths exceeding 1 m were not included in the broad-band array. As a consequence, relatively little benefit was obtained from the broadband array below 80 Hz. Only a few acoustic modes are expected below 100 Hz for the cylinder geometry studied here, and modification of the wall admittance caused shifting of individual modes into and out of adjacent bands. For example, changing the wall admittance to account for the resonator array shifted the first circumferential mode (near 75 Hz) from the 80 Hz to the 63 Hz bands. This produced a small negative NR in the 63 Hz band, as seen in Figure 8. Above 80 Hz, the NR values increased to a peak around 125 Hz.

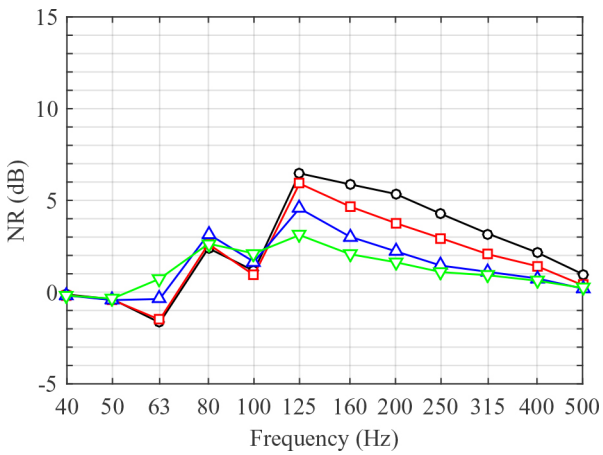

Figure 8. NR attributed to the broadband resonator array during harmonic point excitation for foam treatments with thicknesses of 25.4 mm (○), 50.8 mm (□), 101.6 mm (△), and 152.4 mm (▽).

For example, up to 6 dB of NR was achieved by the resonators in the 25.4 mm thick foam treated cylinder. However, the relative benefit of the resonator array was generally reduced with increasing foam thickness. Also, because foam layers perform better at higher frequencies, the relative benefit of the resonator array was reduced with increasing frequency beyond 125 Hz for all foam thicknesses.

It was also of interest to view the relative NR provided by the foam blankets with closed resonator inlets. Figure 9 shows results similar to Figure 8, but in this case the NR is due to increasing the foam blanket thickness relative to the thinnest blanket considered (25.4 mm) with resonator inlets remaining closed throughout. Needless to say, the thicker blankets provide increased NR overall and perform better at lower frequencies than the thinner treatments. For the highest thickness considered (152.4 mm), the relative NR is upward of 10 dB in bands with appreciable modal content. However, it is important to note that the 50.8 mm, 101.6 mm, and 152.4 mm blankets reduce the interior volume by approximately 4%, 11%, and 18%, respectively, and increase the overall area density of the cylinder sidewall by approximately 2%, 6%, and 10% relative to the thin 25.4 mm blanket. The resonator array takes up no interior volume and contributes no appreciable mass.

Next, the results from the random diffuse field loading are considered. Figure 10 shows an example of the mean interior sound pressure levels resulting from the 50.8 mm thick foam blanket configuration. Results are shown in terms of the mean and envelope of $\langle L_p \rangle$ over the ensemble of diffuse field instances. The peak near 75 Hz is due to the first circumferential mode of the interior. Only a slight reduction is achieved by the resonator array for this mode as it lies below the targeted 100 Hz to 500 Hz frequency range of the resonator array. However, significant reductions in $\langle L_p \rangle$ are achieved above 100 Hz.

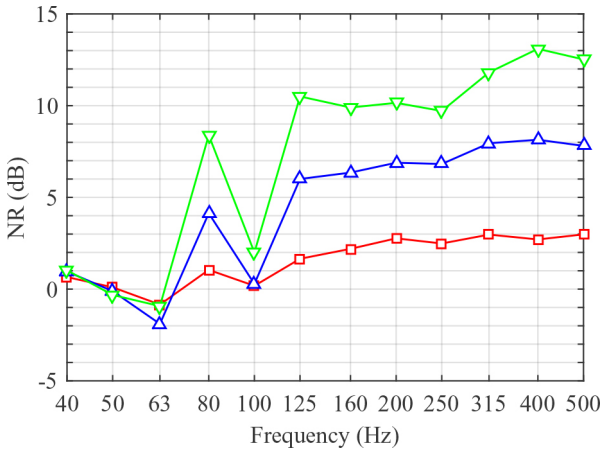

Figure 9. NR attributed to increasing foam thickness to 50.8 mm (□), 101.6 mm (△), and 152.4 mm (▽) relative to 25.4 mm during harmonic point excitation.

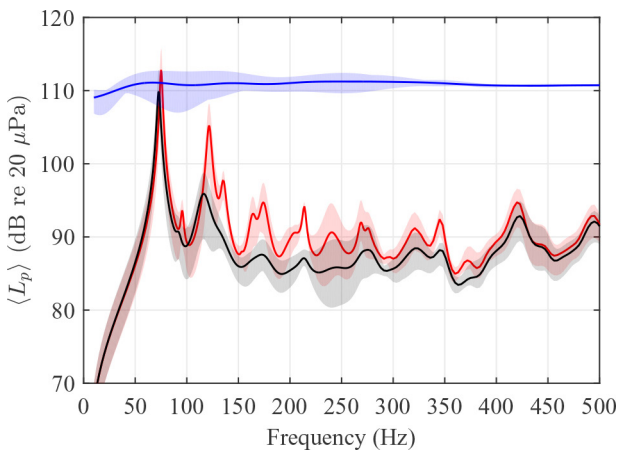

Figure 10. Mean interior sound pressure level $\langle L_p \rangle$ of the 50.8 mm thick foam treated cylinder with (▬) and without (▬) application of the broadband resonator array. The excitation pressure applied to the cylinder exterior is also shown (▬). Shaded regions denote the envelope of results.

Figures 11 and 12 show relative NR spectra due to the broadband resonator array and several foam thicknesses for the diffuse field case. The takaways here are similar to the previous point load results. However, the relative NRs for both the resonator array and foam blankets are slightly greater for the diffuse field load case than for the point load case. One explanation for this is that the diffuse field tends to excite nearly all of the interior modes efficiently, while the point force does so to a lesser extent due to how the resulting cylinder response couples to the interior, which results in the damping of fewer interior modes.

Finally, results from the multitone monopole sources are considered. Figure 13 shows the mean sound pressure levels with and without the multitone resonator array in the 25.4 mm thick foam blanket treated cylinder as an example. The resonators provide significant attenuation near the second and higher tones, while only slight attenuation is seen

at frequencies away from the tones. For example, the 170 Hz tone is reduced by 16 dB. As seen in previous results, the relative benefit of the resonators is reduced with increasing frequency as the foam performance increases. The first excitation tone is largely unaffected by the resonators due to a lack of interior modes in the vicinity of 85 Hz, although the response at the first circumferential mode near 75 Hz is reduced by 3-4 dB. This demonstrates the need to consider interior modes in addition to excitation when designing the resonator array, especially for systems exhibiting low modal density. For example, the 85 Hz tuned resonators in this multi-tone array design may have been more effective if reconfigured to attenuate other tones or interior resonances.

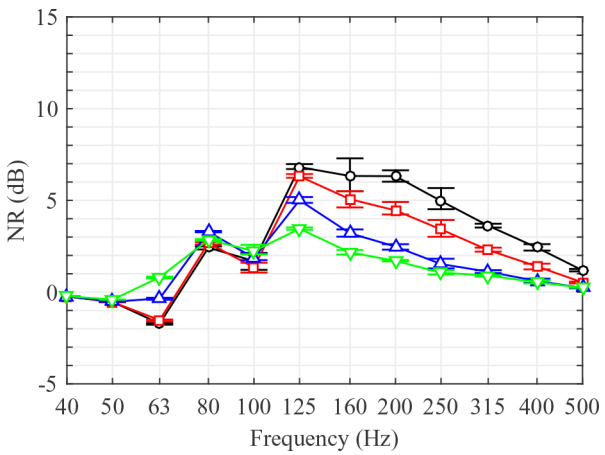

Figure 11. NR attributed to the broadband resonator array during diffuse field excitation for foam treatments with thicknesses of 25.4 mm (○), 50.8 mm (□), 101.6 mm (△), and 152.4 mm (▽). Error bars denote envelope of results.

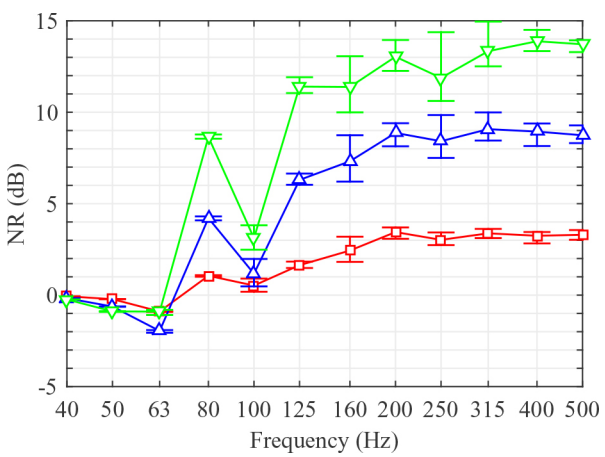

Figure 12. NR attributed to increasing foam thickness to 50.8 mm (□), 101.6 mm (△), and 152.4 mm (▽) relative to 25.4 mm during diffuse field excitation. Error bars denote envelope of results.

The 1/3 octave NR spectra for the multitone excitation cases are also shown in Figures 14 and 15. The results show trends similar to previous results, except in this case the resonators do not provide much attenuation until the 160 Hz 1/3 octave band, which includes the first tone that interacts with interior modes. Also, the NR attributed to increasing foam thickness is similar to previous trends, but apparently varied by the shape of the excitation spectrum and degree to which the multitone pressure field couples with interior modes. While the design of a multitone array may be complicated by system mode interaction, the results suggest that high NR is achievable when targeting specific frequencies as evidenced by the 160 Hz 1/3 octave band NR of ~15 dB for the thin foam blanket configuration.

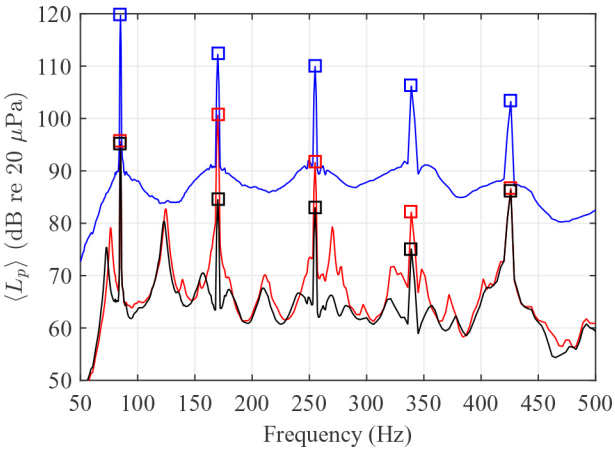

Figure 13. Mean interior sound pressure level $\langle L_p \rangle$ of the 25.4 mm thick foam treated cylinder with (—) and without (—) application of the multitone resonator array. The mean excitation pressure applied to the cylinder exterior is also shown (—). Boxes denote the multitone peaks.

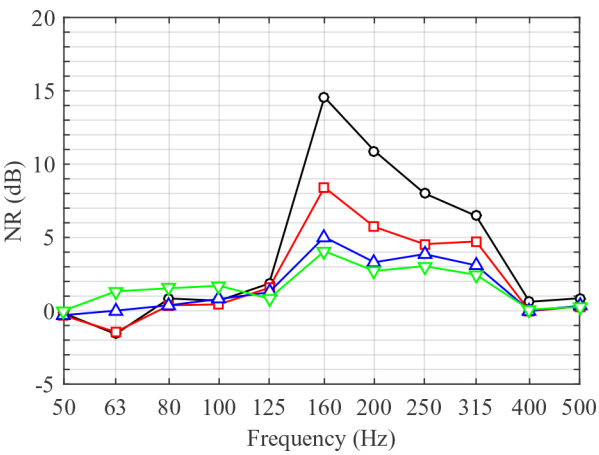

Figure 14. NR attributed to the multitone resonator array during harmonic multitone excitation for foam treatments with thicknesses of 25.4 mm (○), 50.8 mm (□), 101.6 mm (△), and 152.4 mm (▽).

Discussion

Experiments on similar flat panel resonator array systems have shown that resonators can reduce noise through increased absorption and reduced transmission, and the noise control capabilities of porous media blankets are well known. The purpose of this analysis was to demonstrate the noise control capability of these two types of treatments when combined in a cylindrical enclosure representative, albeit simplistically, of a flight vehicle fuselage section. The primary takeaway is that the resonator array NR is reduced as foam blanket NR increases. While the integrated resonators are known to contribute to NR in the form of insertion loss (reduced transmission), the trade-off between the two treatments can be largely attributed to relative changes in the interior absorption area. In the context of room acoustics, the room NR due to a change in absorption area is $10\log_{10}((A_0 + A_t)/A_0)$, where A_0 and A_t are respectively the baseline and

additional treatment absorption areas. This simplified expression neglects changes in transmission loss, direct field contribution, and strong low frequency modal behaviour in enclosed vibroacoustic systems, but it can be useful to understand the relative influence of a treatment. Specifically, as A_0 increases, At has less effect.

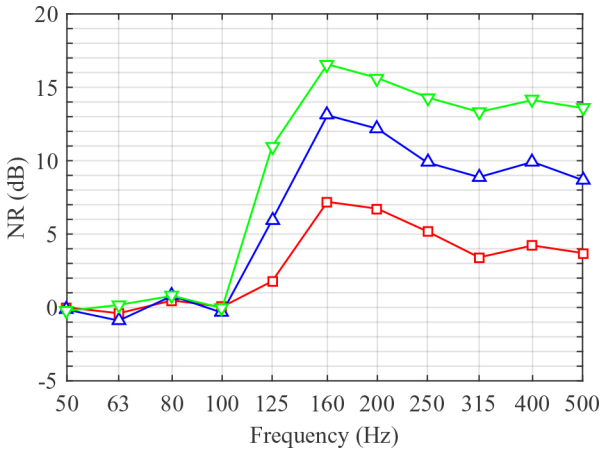

Figure 15. NR attributed to increasing foam thickness to 50.8 mm (□), 101.6 mm (△), and 152.4 mm (▽) relative to 25.4 mm during harmonic multitone excitation.

In light of this, the benefit of integrated resonators is not necessarily related to their noise control capability alone, but in their ability to reduce the workload of conventional treatments at low frequencies. In other words, supplementation of the noise control system below, say, 500 Hz with integrated resonators may allow for the use of very thin blanket treatments while still meeting the overall noise requirement.

CONCLUSIONS

Using numerical models of an aerospace-relevant cylindrical vibroacoustic system, the relative and combined noise control capability of conventional foam blanket treatments and integrated resonator arrays were evaluated. The metric of interest was the cylinder interior space-averaged sound pressure level. A few exterior excitations were considered during direct frequency response analyses, including a harmonic point force, a harmonic multitone pressure field, and a random diffuse pressure field. Different thicknesses of foam blanket treatments were considered to gain insight into the combined performance of the integrated resonator arrays with various degrees of conventional treatment. The results suggest that structurally integrated resonator arrays can be effectively used in conjunction with conventional foam blanket noise treatments and tailored to suit a variety of noise control requirements, but their relative benefit diminishes if outperformed by other treatments.

REFERENCES

1. Junger M. C., “Helmholtz resonators in load-bearing walls,” *Noise Control Engineering*, vol. 4, pp. 17-25, Jan. 1975.
2. Jones M. G. and Howerton B. M., “Evaluation of parallel-element, variable-impedance, broadband acoustic liner concepts,” in Proceedings of the 18th AIAA/CEAS Aeroacoustics Conference, (Colorado Springs, CO), June 2012.
3. Mason J. M. and Fahy F. J., “The use of acoustically tuned resonators to improve the sound transmission loss of double-panel partitions,” *Journal of Sound and Vibration*, vol. 124, pp. 367-379, 1988.
4. Prydz R. A., Wirt L. S., Kuntz H. L., and Pope L. D., “Transmission loss of a multilayer panel with internal tuned Helmholtz resonators,” *Journal of the Acoustical Society of America*, vol. 87, pp. 1597-1602, 1990.
5. Kuntz H. L., Gatineau R. J., Prydz R. A., and Balena F. J., “Development and testing of cabin sidewall acoustic resonators for the reduction of cabin tone levels in propfanpowered aircraft,” Tech. Rep. CR 4388, NASA, 1991.
6. Li D. and Vipperman J. S., “Noise control of mock-scale chambercore payload fairing using integrated acoustic resonators,” *Journal of Spacecraft and Rockets*, vol. 43, pp. 877-882, 2006.
7. Lane S. A., Henderson K., Williams A., and Ardelean E., “Chamber core structures for fairing acoustic mitigation,” *Journal of Spacecraft and Rockets*, vol. 44, pp. 156-163, 2007.
8. Schiller N. and Allen A., “Tuned chamber core panel acoustic test results,” Tech. Rep. TM 2016-219338, NASA Langley Research Center, 2016.
9. *ABAQUS version 6.14 Documentation, ABAQUS Analysis User’s Manual*. Providence, RI, 2014.
10. Miki Y., “Acoustical properties of porous materials - modifi-cations of Delany-Bazley models,” *Journal of the Acoustical Society of Japan*, vol. 11, pp. 19-24, 1990.
11. Allen A. R. and Schiller N. H., “Experimental evaluation of equivalent-fluid models for melamine foam,” in Proceedings of NoiseCon 2016, (Providence, RI), June 2016.
12. Lok T.-S. and Cheng Q.-H., “Elastic stiffness properties and behavior of truss-core sandwich panel,” *Journal of Structural Engineering*, vol. 126, pp. 552-559, 2000.
13. Pierce A. D., *Acoustics: An Introduction to Its Physical Principles and Applications*. Acoustical Society of America, 1991.
14. Coyette, J., Detandt, Y., Lielens, G., and Van den Nieuwenhof, B., "Vibro-Acoustic Simulation of Mechanical Components Excited by Distributed Random Loads," SAE Technical Paper 2009-01-2212, 2009, doi:10.4271/2009-01-2212.
15. Rafaely B., “Spatial-temporal correlation of a diffuse sound field,” *Journal of the Acoustical Society of America*, vol. 107, pp. 3254-3258, 2000.
16. ASTM C384, *Standard Test Method for Impedance and Absorption of Acoustical Materials by Impedance Tube Method*, 2004.

APPENDIX

To validate the resonator impedance model, predictions are compared with normal incidence impedance measurements collected on a representative sandwich structure. The sandwich structure, shown in Figure 16, has a fluted core with a core period of 50.8 mm and chamber thickness of 16.5 mm. Expanded polyethylene foam plugs were inserted into the core to seal the chambers and repositioned to achieve different cavity lengths. A variety of inlet radii were machined in the top face to assess the impedance sensitivity to inlet size.

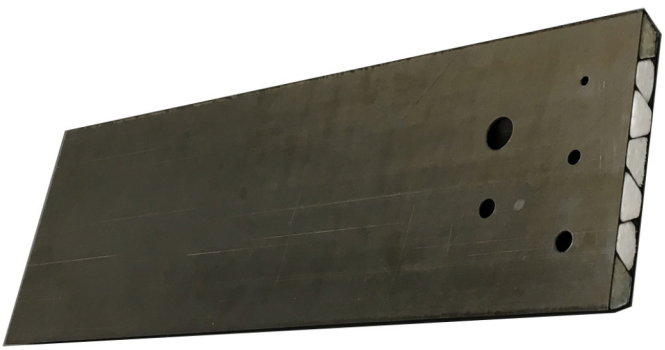

Figure 16. Fluted core test article containing 5 resonators with varied inlet radii and adjustable chamber lengths.

Impedance measurements were carried out using a 50.8 mm by 50.8 mm normal incidence tube apparatus[§]. During the tests, the impedance tube was positioned above one of the inlets and excited with broadband noise from 50 to 1500 Hz with an overall sound pressure level of 120 dB. The two-microphone technique was then used to determine the input impedance at the face of the test article including one resonator inlet [16]. Because the area of the resonator inlet was smaller than the cross-section area of the impedance tube, z_r was determined from the measured impedance by considering the area weighted average of the specific acoustic admittance over the entire test surface

$$z_r = \left(\frac{y_w S_w + y_r S_i}{S_w + S_i} \right)^{-1}, \tag{8}$$

where y_w and S_w refer respectively to the admittance and surface area of the test article face sheet and y_r and S_i correspond to the admittance at the resonator inlet and the inlet area. The admittance of the face sheet was assumed to be 0 m/(Pa·s).

Figure 17 shows comparisons between measurements and predictions for three different resonator lengths and three different inlet diameters. The input parameters used in the predictions are given in Table 2. A resistance value of R = 2 MKS Rayl in addition to the wide-duct losses was found to improve correlation with measurements.

Table 2. Parameters used for model results shown in Figure 17.

ρ	1.21 kg/m^3
c	343 m/s
γ	1.4
Pr	0.71
μ	1.81E-5 Pa·s
R	2 MKS Rayl
S_c	4.19E-4 m^2
L_c	279 mm, 368 mm, 495 mm
S_i	1.27E-4 m^2, 0.71E-4 m^2, 0.28E-4 m^2

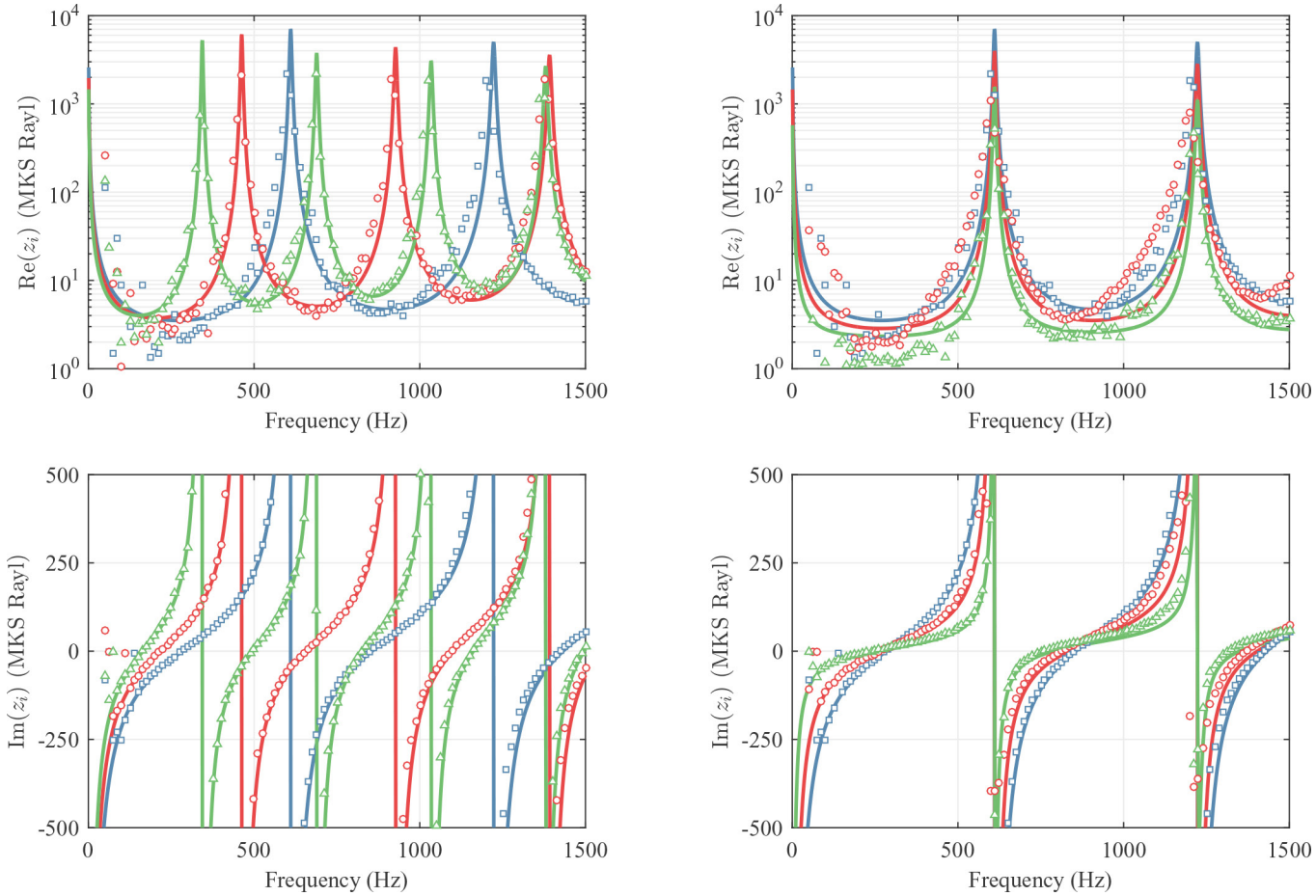

Figure 17. Left: Real and imaginary components of the inlet impedance for resonators with inlet diameter = 12.7 mm and L_c = 279 mm (□, —), 368 mm (○, —), and 495 mm (△, —). Right: Real and imaginary components of the inlet impedance for resonators with L_c = 279 mm and inlet diameters of 12.7 mm (□, —), 9.5 mm (○, —), and 6.0 mm (△, —). Measured values are shown with symbols and model results with lines.